Geochemistry, Geophysics, Geosystems®

AGU ADVANCING EARTH AND SPACE SCIENCE

RESEARCH ARTICLE
10.1029/2022GC010730

Key Points:

- Magnetic measurements delineate carbonation processes and extent in peridotite
- We observe a correlation between magnetic signal and in situ carbonation process
- Fluid chemistry and flow mode impact magnetic signal of incipient carbonation

Supporting Information:

Supporting Information may be found in the online version of this article.

Correspondence to:

M. Tominaga,
mtominaga@whoi.edu

Citation:

Tominaga, M., Beinlich, A., Lima, E. A., Pruett, P., Vento, N. R., & Weiss, B. P. (2023). High-resolution magnetic-geochemical mapping of the serpentinized and carbonated Atlin ophiolite, British Columbia: Toward establishing magnetometry as a monitoring tool for in situ mineral carbonation. *Geochemistry, Geophysics, Geosystems*, *24*, e2022GC010730. https://doi.org/10.1029/2022GC010730

Received 5 OCT 2022
Accepted 3 MAR 2023

Author Contributions:

Conceptualization: Masako Tominaga, Andreas Beinlich
Data curation: Masako Tominaga, Andreas Beinlich, Paiden Pruett, Noah R. Vento
Formal analysis: Masako Tominaga, Andreas Beinlich, Eduardo A. Lima, Paiden Pruett, Noah R. Vento
Funding acquisition: Masako Tominaga, Benjamin P. Weiss

High-Resolution Magnetic-Geochemical Mapping of the Serpentinized and Carbonated Atlin Ophiolite, British Columbia: Toward Establishing Magnetometry as a Monitoring Tool for In Situ Mineral Carbonation

Masako Tominaga[1], Andreas Beinlich[2], Eduardo A. Lima[3], Paiden Pruett[4], Noah R. Vento[4], and Benjamin P. Weiss[3]

[1]Department Geology and Geophysics, Woods Hole Oceanographic Institution, Woods Hole, MA, USA, [2]Department of Earth Science, Center for Deep Sea Research, University of Bergen, Bergen, Norway, [3]Department of Earth, Atmospheric and Planetary Sciences, Massachusetts Institute of Technology, Cambridge, MA, USA, [4]Department of Geology and Geophysics, Texas A&M University, College Station, TX, USA

Abstract We address in situ serpentinization and mineral carbonation processes in oceanic lithosphere using integrated field magnetic measurements, rock magnetic analyses, superconducting quantum interference device (SQUID) microscopy, microtextural observations, and energy dispersive spectroscopy phase mapping. A representative suite of ultramafic rock samples were collected, within the Atlin ophiolite, along a 100-m long transect across a continuous outcrop of mantle harzburgite with several alteration fronts: serpentinite, soapstone (magnesite + talc), and listvenite (magnesite + quartz). Strong correlations between changes in magnetic signal strengths and amount of alteration are shown with distinctive contrasts between serpentinite, transitional soapstone, and listvenite that are linked to the formation and breakdown of magnetite. While previous observations of the Linnajavri ultramafic complex indicated that the breakdown of magnetite occurred during listvenite formation from the precursor soapstone (Tominaga et al., 2017, https://doi.org/10.1038/s41467-017-01610-4), results from our study suggest that magnetite destabilization already occurred during the replacement of serpentinite by soapstone (i.e., at lower fluid CO_2 concentrations). This difference is attributed to fracture-controlled flow of sulfur-bearing alteration fluid at Atlin, causing reductive magnetite dissolution in thin soapstone zones separating serpentinite from sulfide-mineralized listvenite. We argue that magnetite growth or breakdown in soapstone provides insight into the mode of fluid flow and the composition, which control the scale and extent of carbonation. This conclusion enables us to use magnetometry as a viable tool for monitoring the reaction progress from serpentinite to carbonate-bearing assemblages in space and time with a caution that the three-dimensionality of magnetic sources impacts the scalability of measurements.

Plain Language Summary Magnetic remote sensing has been used in unlocking otherwise inaccessible information about geodynamic processes. Here, we expand and use magnetometry to monitor in situ mineral carbonation processes in mantle peridotite, one of the major rock formations that compose this planet Earth. We conducted integrative magnetometry-geochemistry observations in the field and lab using magnetic measurements, rock magnetic analyses, superconducting quantum interference device microscopy, microtextural observations, and energy dispersive spectroscopy phase mapping. Based on results from this integrative approach, we observe a correlation between magnetic signal and in situ carbonation process. This observation supports the idea that magnetic measurements can delineate carbonation extent and degree in peridotite alteration processes. We also observe that fluid chemistry and flow mode impact the magnetic signal of incipient carbonation. Altogether, our study enables us to further use magnetometry results in monitoring in situ peridotite carbonation, and possibly, the mode of fluid flows during the chemical process.

1. Introduction

Magnetic remote sensing has been used in unlocking otherwise inaccessible information about geodynamic processes. Changes in magnetic anomalies, and magnetization distribution as inferred from magnetic data inversion, emerge from one or a combination of the contrast between geomagnetic polarity reversals at the time of remanence acquisition, source geometry/structural contrast (e.g., faults), and/or variations in magnetic carriers and rock composition. Inverse modeling of magnetic signals is applied to decipher crustal architecture, the nature

Investigation: Masako Tominaga, Andreas Beinlich, Paiden Pruett, Noah R. Vento
Methodology: Masako Tominaga, Andreas Beinlich
Project Administration: Masako Tominaga
Resources: Masako Tominaga, Andreas Beinlich, Eduardo A. Lima, Benjamin P. Weiss
Supervision: Masako Tominaga
Validation: Masako Tominaga, Andreas Beinlich, Eduardo A. Lima
Visualization: Masako Tominaga, Andreas Beinlich, Eduardo A. Lima, Paiden Pruett, Benjamin P. Weiss
Writing – original draft: Masako Tominaga
Writing – review & editing: Andreas Beinlich, Eduardo A. Lima, Paiden Pruett, Noah R. Vento, Benjamin P. Weiss

and distribution of mineral deposits, and global plate tectonics (e.g., Galley et al., 2020; Maffione et al., 2014; Szitkar et al., 2014).

Recent studies suggested that the extent and mode of metasomatic processes, including serpentinization and carbonation of mantle rocks, could be effectively monitored in situ through changes in rock magnetic properties resulting from the production and replacement of magnetite that controls crystallization remanent magnetization (e.g., Cutts et al., 2021; Tominaga et al., 2017). In the world's oceans, mantle rocks are exposed on the seafloor at slow and ultraslow spreading mid-ocean ridges that account for ∼30% of today's active ridge system (e.g., Cannat, 1996). Delineating the rate and extent of serpentinization and carbonation of mantle rock within the oceanic lithosphere is fundamental for advancing an understanding of the effect of hydrothermal processes on rock physical properties such as rheology and density and for constraining the feedstock availability for geological CO_2 sequestration (e.g., Beinlich et al., 2012; Kelemen & Matter, 2008; Kelemen et al., 2022; Szitkar et al., 2014). It also has a significant implication for the existence of deep biosphere (e.g., Daae et al., 2013; Jørgensen & Zhao, 2016).

However, there have only been a small number of studies using magnetic remote sensing to delineate subsurface serpentinization and mineral carbonation. Particularly limited are studies that investigate the temporal variation and complexity of crystallization remanent magnetization based on spatially separated alteration zones that represent snapshots of propagating rock alteration fronts. Current knowledge about peridotite serpentinization and mineral carbonation is largely based on purely petrologic and geochemical field observations, thermodynamic modeling, and experimental studies (e.g., Bach et al., 2006; Beinlich & Austrheim, 2012; Frost, 1985; Kelemen & Matter, 2008; Klein & Garrido, 2011; Krevor & Lackner, 2011; McCollom & Bach, 2009; Plümper et al., 2014). There are only a few magnetometry studies in ophiolites (e.g., Airo, 2002; Cutts et al., 2021; Michels et al., 2018; Tominaga et al., 2017) that focused on bridging the scales from laboratory analyses to field observations. However, the link between magnetic signals and in situ chemical processes requires further investigation for establishing magnetometry as a monitoring tool for in situ chemical processes. As a next step, it is essential to understand how fluid flow and the resulting metasomatic alteration, and thereby crystallization remanent magnetization of rock, affect magnetic signals. Closely investigating a well-exposed outcrop with a spatially continuous section of variably serpentinized and carbonated rocks could provide a key understanding of the reactions progress during active alteration in situ and their evolution as a magnetic source.

In this study, we address the applicability of magnetic measurements for understanding serpentinization and carbonation processes in situ, using observations from a fragment of ancient seafloor that is now exposed at the Atlin ophiolite, British Columbia, Canada (Figure 1). We report the results from a comprehensive suite of rock magnetic analyses, superconducting quantum interference device (SQUID) magnetic microscopy, petrological observations, and geochemical mapping of representative rock samples. The samples for this study were systematically collected along a survey transect that allows us to characterize the effects of hydrothermal hydration and carbonation of oceanic lithosphere on rock magnetic properties (Figure 1), thus complementing previous insights gained at the Linnajavri ultramafic complex, Norway (Tominaga et al., 2017). Our observations show that the mode of hydrothermal alteration results in distinct magnetic fingerprints dictated by the alteration degree and distribution within the investigated rock formation.

2. Geological Background

2.1. Geodynamic History of the Atlin Ophiolite

The Atlin ophiolite is an upper mantle section of the Tethyan oceanic lithosphere and part of the regional Cache Creek terrane of the Canadian Cordillera. The Cache Creek terrane is interpreted as an exotic block comprising oceanic uppermost mantle, crustal and sedimentary rocks accreted to the adjacent Stikinia and Quesnellia arcs during the Middle Jurassic (∼165 Ma) followed by Lower Cretaceous (∼140 Ma) amalgamation with the North American plate (Ash & Arksey, 1990; Johnston & Borel, 2007). The stratigraphic relationships between Cache Creek seamounts, Paleozoic to Jurassic shallow to deep-water chemical and clastic sedimentary rocks, and Triassic conglomerates suggest that the oceanic fragments of the Cache Creek terrane formed at spreading ridges in the Paleo-Tethys on the eastern side of the South Chinese Crustal Block (Johnston & Borel, 2007). The North America plate reconstruction model suggests that the Cache Creek terrane's paleolatitude remained near its current location from the time of accretion (Matthews et al., 2016; Müller et al., 2018; See also Figure S1 in Supporting Information S1).

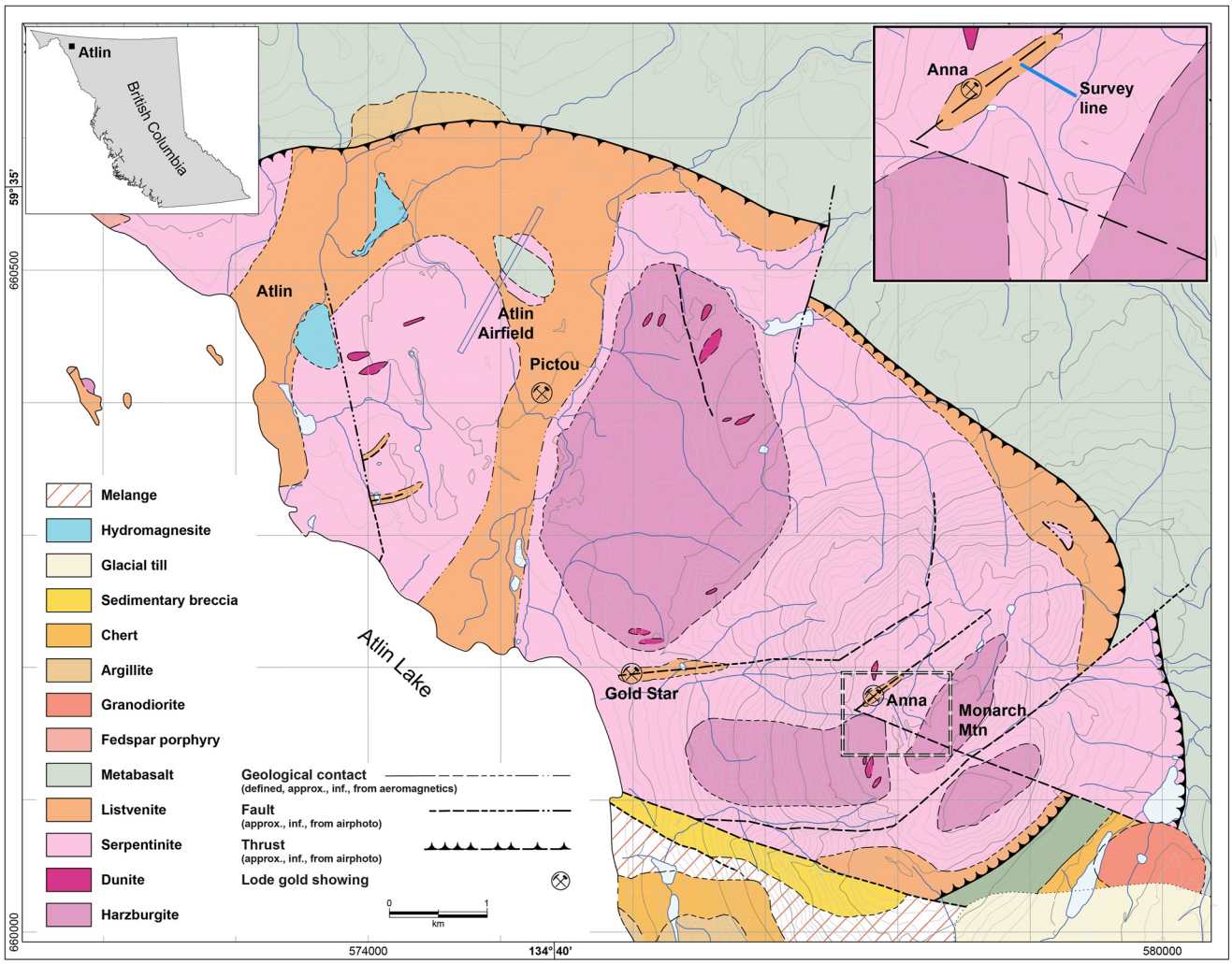

Figure 1. Geological map of the Atlin ophiolite (after Ash, 1994). The upper left inset shows the location of Atlin in relation to British Columbia. The upper right inset shows the location of our survey transect near the Anna Au showing on top of Monarch Mountain. In the inset, red, purple, pink, and orange colors indicate dunite, harzburgite, serpentinite, and listvenite, respectively. See Figure 2 for the imagery of sampling sites along the survey transect.

The Atlin ophiolite is predominantly composed of harzburgite with subordinate dunite, and is variably altered to serpentinite and listvenite (Ash & Arksey, 1990; Hansen et al., 2005). In few places, additional soapstone is present as thin and spatially isolated transitional alteration assemblage. In the serpentinite, fault and the alignment of bastite alteration zones after primary orthopyroxene with penetrative S2 foliation fabric, both of which crosscut the primary magmatic fabric, indicates syn-deformational alteration, potentially coeval with the obduction of the ophiolite (Ash, 1994). The intensity of the S2 foliation fabric varies from weak to localized mylonitic high-strain zones. Such high-strain zones are present near the tectonic margins of the ophiolite and at the western side of Monarch Mountain along a prominent east-trending normal fault. The latter hosts the Gold Star lode gold occurrence and is surrounded by a well-developed alteration halo where the deformed and serpentinized harzburgite is pervasively altered to listvenite (Figure 1) (Ash, 1994; Ash & Arksey, 1990).

The spatial relationship between deformation structures, mineralization, and the location of serpentinite and listvenite indicates that the Atlin ophiolite underwent multiple episodes of hydrothermal alteration by aqueous and carbon-bearing fluids and constrains the timing of CO_2-bearing fluid flow to the waning stage of ophiolite obduction or later. This is consistent with the 161–174 Ma ^{40}Ar-^{39}Ar age range of Cr-muscovite after primary Cr-spinel sampled at several of the Atlin gold showings, one of which is from the Anna location near our survey site (Figure 1) (Ash, 1994, 2001), and the 210–280°C fluid inclusion temperature range obtained from listvenite-hosted quartz-carbonate veins (Andrew, 1985). The source of the fluids for mineralization and carbonation is difficult to

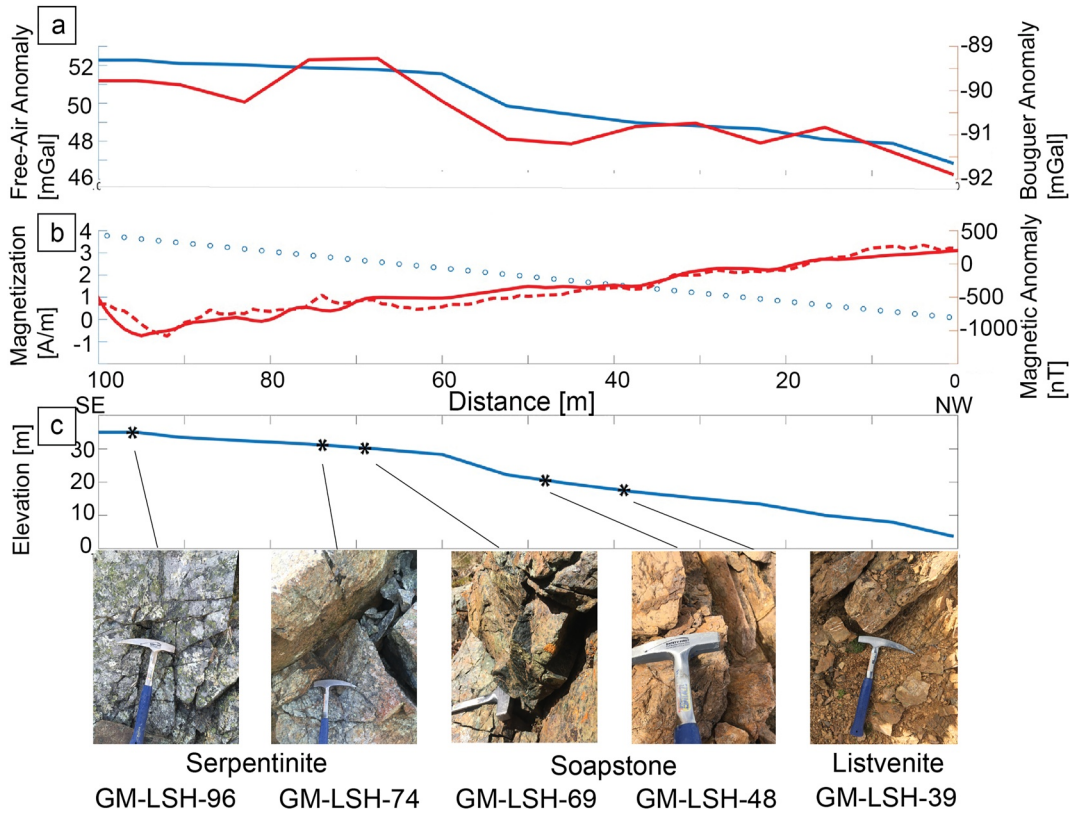

Figure 2. Summary of the field survey along the 100 m transect at Monarch Mountain, Atlin. (a) Crustal scale gravity (top: free air (blue) Bouguer (red) anomalies, with 2.67 g/cm^3 reduction density (See Text S1 in Supporting Information S1).) and (b) magnetic anomaly measurements (observed (red dotted; nT) and forward model results (red solid; nT) based on magnetization model (blue circles, Am^2)). (c) Changes in elevation over the survey transect. All measurements were taken with a 1 m sampling interval. The stars indicate the locations of the five representative rock samples shown in the imagery.

precisely constrain. However, Ash (2001) suggested amphibolite-facies dehydration of local metasediments, deep circulation of meteoric water, and possibly magmatic fluids related to the 172 ± 3 Ma Fourth of July Batholite (Mihalynuk et al., 1992) ~4 km to the north of the Atlin ophiolite. Extensive hydromagnesite-magnesite playas in the surrounding wetlands are formed by current weathering of the Atlin ophiolite (e.g., Mavromatis et al., 2021; Power et al., 2014).

2.2. Magnetic Understanding of Serpentinization and Carbonation of Mantle Peridotite

Peridotite is the dominant rock type of the upper ~400-km of the Earth's mantle and consists of more than 60 vol.% of the mineral olivine ($(Mg,Fe)_2SiO_4$) with additional pyroxene ($(Ca, Mg, Fe)_2Si_2O_6$). Peridotite is exposed along slow and ultraslow mid-ocean ridge spreading centers, oceanic core complexes (e.g., Cannat, 1996), and different forms occur in the continental crust as intrusions and within ophiolites. Peridotite is readily altered in the presence of reactive fluid via dissolution of the primary silicate minerals and subsequent precipitation of the secondary silicate and/or carbonate minerals, depending on the fluid composition and alteration pressure and temperature. Under typical subseafloor alteration conditions (i.e., temperature, $T \lesssim 400$°C, pressure, $P \lesssim 6$ kbar, reaction-buffered oxygen fugacity, fO_2, silica activity, $aSiO_{2,aq}$, and low carbon dioxide activity, $aCO_{2,aq}$), peridotite alteration by aqueous fluids results in the formation of secondary serpentine ($(Mg,Fe)_3Si_2O_5(OH)_4$) and brucite ($(Mg,Fe)(OH)_2$). At temperatures above 200°C, serpentinization is further accompanied by the formation of abundant magnetite ($Fe_2^{3+}Fe^{2+}O_4$), which drives the formation of molecular hydrogen (H_2) that has been thought to provide an important energy source for deep-sea microorganisms (e.g., Klein et al., 2014; Maffione et al., 2014; Malvoisin et al., 2012). The reducing conditions prevailing during serpentinization frequently result also in the formation of metallic alloys (for example, awaruite ($Ni_{2-3}Fe$)) and native metals (e.g., Frost, 1985; Lorand, 1987; Plümper et al., 2014). Tectonic emplacement of ultramafic oceanic lithosphere onto continental

crust commonly involves alteration by fluids that have previously been in contact with carbon-bearing continental rocks and sediments and hence are CO_2-bearing. Such alteration results in the formation of assemblages containing carbonate minerals (calcite ($CaCO_3$), dolomite $CaMg(CO_3)_2$, magnesite ($MgCO_3$)) in addition to talc ($Mg_3Si_4O_{10}(OH)_2$) and/or quartz (SiO_2) that are rare or even absent from pristine seafloor serpentinite (Bach et al., 2006; Beinlich et al., 2012; Beinlich, Plümper, et al., 2020; Frost, 1985; Frost & Beard, 2007; Hansen et al., 2005; Klein & Garrido, 2011; Klein et al., 2009; Menzel et al., 2020). Depending on the concentration of dissolved carbon at given temperature and pressure, peridotite carbonation by COH-fluids results in different alteration assemblages termed ophimagnesite (magnesite + serpentine), soapstone (magnesite + talc), and listvenite (magnesite + quartz)—in order of increasing fluid carbon concentration. Additional minor phases (e.g., tremolite) may form depending on protolith composition and mass-transport during the alteration.

Fe initially in the primary olivine will partition into secondary minerals depending on the alteration conditions and the Fe-Mg exchange potential that dictates a general preference for Fe in the order olivine > serpentine > talc (e.g., Frost & Beard, 2007; Trommsdorff & Evans, 1972). Consequently, the replacement of olivine by serpentine, of serpentine by talc and magnesite (i.e., soapstone) and then by quartz and magnesite (i.e., listvenite) is supposed to result in the formation of additional one or more Fe-bearing phases. Typically, the Fe-rich phase is magnetite unless elevated f_{O_2} in relatively shallow alteration settings stabilizes hematite ($Fe^{3+}_2O_3$) and/or goethite ($Fe^{3+}O(OH)$). Hence, peridotite carbonation to soapstone and listvenite is theoretically expected to increase the rock's magnetite content, and consequently also its magnetic susceptibility and remanent magnetization. However, some previous observations do not support this prediction (Airo, 2002; Ash & Arksey, 1990; Hansen et al., 2005). Tominaga et al. (2017) presented magnetic and textural observations for the breakdown of magnetite and formation of Fe-enriched magnesite resulting in a distinct decrease in magnetic field strength during the most intense carbonation that is consistent with those previous observations (Airo, 2002; Ash & Arksey, 1990; Hansen et al., 2005). Tominaga et al. (2017) suggested that listvenite formation is associated with the formation of nonmagnetic minerals at the expense of magnetite, most likely aided by reductive dissolution of magnetite through the presence of dissolved sulfur species in the reactive fluid.

The formation and then breakdown of magnetite during progressive peridotite alteration in both oceanic and continental settings have been recognized to change the magnetic properties of the rock (Hansen et al., 2005; Malvoisin et al., 2012; Tominaga et al., 2017). These changes are intrinsically related to the timing of acquisition and stability of the rock's magnetic natural remanent magnetization (NRM). In the case of serpentinite, most of the characteristic remanence is crystallization remanent magnetization (Dunlop & Özdemir, 1997) acquired by the formation of magnetite during the serpentinization (e.g., Malvoisin et al., 2012; Oufi et al., 2002). This remanent magnetization has been recognized as a source of magnetic anomalies within slow- and ultraslow-spreading seafloor and ophiolites, including the Atlin ophiolite (e.g., Ash & Arksey, 1990). The NRM of such serpentinite samples has been found to have a smaller median destructive field than that of basalts, probably related to the larger grain size of the magnetic carrier minerals (e.g., Maffione et al., 2014; Malvoisin et al., 2012). However, it has rarely been documented and discussed how the crystallization remanence magnetization of serpentinized ultramafic rocks changes during subsequent carbonation reactions, despite the observed breakdown of magnetite and associated reduction in magnetic signal strengths (e.g., Cutts et al., 2021; Tominaga et al., 2017).

3. Methods

3.1. Field Relationships and Petrology

Our survey was primarily conducted along a 100 m long transect line across a continuous outcrop of mantle peridotite at Monarch Mountain, Atlin (59.5408°N, 133.6081°W) (as measured by a handheld GPS with accuracy of ±5–10 m) (Figure 1). The survey line transects zones of pervasive alteration of the precursor harzburgite to serpentinite, and additional talc-magnesite (soapstone), and quartz-magnesite (listvenite) zones. While the degree of serpentinization is difficult to determine in the field, the presence of carbonate is accompanied by a distinctive color change from dark gray to rusty brown and allows for precise distance measurement of the carbonation front at ∼39 m from the origin of the survey transect. Besides this obvious change in mineral content of the rock, the surface exposure along our survey line lacks visual evidence for rock heterogeneity.

Five representative unoriented rock samples were taken along the transect for chemical and microtextural analyses as well as SQUID magnetic microscopy. These represent the serpentinized harzburgite (GM-LSH-96 and

-74), soapstone (GM-LSH-69), and listvenite (GM-LSH-48 and 39) (Figure 2c). SQUID microscopy analyses were performed on 30 μm thin sections made from each sample made with cyanoacrylate cement and without heating to preserve the NRM. The same thin sections were also used for subsequent chemical and textural analyses. The order in which magnetic and chemical analyses were performed ensured that the NRM of the thin sections remained undisturbed by other analytical techniques. The hand specimens selected for thin section preparation were subsequently used for bulk rock magnetic analyses.

Full thin section energy disperse spectroscopy (EDS) phase maps were obtained using a TESCAN Integrated Mineral Analyzer (TIMA) high resolution field emission scanning electron microscope (FE-SEM) in full liberation mode and at 3 μm spatial resolution at the John De Laeter Centre, Curtin University, Australia. The operating conditions were 15 keV, 0.8 nA and a working distance of 10 mm. Processing of EDS spectra was done using the TESCAN TIMA software. EDS phase abundance is given in area %, referred to as % in the text. The uncertainty of the relative mineral proportions is estimated at most 5%.

3.2. Crustal Scale Magnetic Field Measurements

We conducted a series of magnetic field measurements along the survey line to detect magnetic anomalies at the meter-scale using a hand-held Applied Physics Systems (APS) 3-axis fluxgate magnetic sensor. We conducted measurements with two ∼2.5 and 1 m sampling intervals for magnetometry, respectively, with at least 3–4 static repeated measurements. The GPS coordinates and altitude of the measurement locations were recorded with a handheld GPS. We also verified these measurements with the Canada digital elevation model (Natural Resources Canada, 2019) to confirm the terrain elevation and overall topography (Figure 2b). The APS magnetometer sensor has a 0.01 nT resolution with 1–20 Hz sampling rates for near-source magnetic mapping.

3.3. Rock Magnetic Measurements

Various rock magnetic experiments were conducted on the 5 lithologically representative samples (GM-LSH-96, -74, -69, -48, and -39) (Figures 2, 4 and 5). All rock magnetic measurements on these samples were conducted at the Institute for Rock Magnetism (IRM) of the University of Minnesota. Room temperature hysteresis measurements were conducted on a Princeton Measurements Vibrating Sample Magnetometer ("VSM2" at IRM) with a sensitivity of 10^{-9} Am^2. The coercivity characteristics of dominant mineral assemblages were determined by first-order reversal curves (FORC) (Figure 4a), hysteresis loops and backfield curves (Figure 4b). A total of 326–414 curves per sample were measured giving a field step width for adjacent FORCs of 100 mT. FORCs were processed using FORCinel (Harrison & Feinberg, 2008) applying a smoothing factor of 10. The Geofyzika KLY-2 KappaBridge alternating current (AC) Susceptibility Bridge was used to measure temperature-dependent susceptibility (TDS) to determine the types of magnetic minerals (Figure 4c). Frequency-dependent susceptibility (FDS) analyses were completed using a superconducting susceptometer (MPMS, "Blue" at IRM) to measure the direct current (DC) zero field cooling/field cooling (ZFC/FC) and AC FDS (Figure 5). FDS measurements were conducted with an AC that records magnetic susceptibility with a changing AC field between 1.0 and 99.9 Hz.

3.4. Scanning SQUID Microscopy

We used the scanning SQUID microscope at the Massachusetts Institute of Technology Paleomagnetism Laboratory to characterize the submillimeter scale (∼200 μm) total magnetic field distribution in the thin sections (Figure 6). The SQUID microscope has ∼0.01 nT sensitivity and measures the vertical component of the magnetic field (i.e., normal to the sample's surface) above polished samples (Weiss et al., 2007). The samples' NRM field was measured on a planar grid ∼200 μm above the thin sections in a planar rectangular grid with a 75 μm spacing. Using the same measurement configuration, we also mapped the thin sections after performing alternating-field (AF) demagnetization up to 145 mT and subsequently imparting anhysteretic remanent magnetization (ARM) with a bias field of 100 μT and a peak alternating field of 145 mT. The purpose of the ARM measurements was two-fold: (a) to magnetize all coercivity phases up to 145 mT; and (b) to assess the maximum magnetic field produced when the sample is uniformly magnetized by a laboratory field with a strength comparable to NRM. This enables us to discern whether spatial variations in the NRM are due to changes in the concentration of magnetic carriers or owing to variations in the efficiency of the magnetization acquisition process. During the SQUID microscopy measurements, we set a higher bias field (100 μT) than the ambient geomagnetic field

Table 1
Mineral Abundance (Area %) in Representative Rock Samples

	GM LSH-96 serpentinite	GM LSH-74 serpentinite	GM LSH-69 soapstone	GM LSH-48 soapstone	GM LSH-39 listvenite
Dolomite	2.8	0.3	4.9	0	0
Magnesite	0	0	5.3	39.3	58.9
Serpentine	88.5	88.9	11.1	4.3	0.9
Talc	7	7.6	78.2	55.7	1.1
Quartz	0	0	0	0	38.5
Chromite	0	0.2	0	0.2	0.3
Magnetite	1.5	3.1	0.4	0.4	0.2
Pentlandite	0.2	0	0	0	0.1
Total (%)	100	100	100	100	100

present at Atlin (~55 nT) to roughly reproduce the magnetization intensity of the sample suite.

On the same set of thin sections, we also conducted AF demagnetization treatment using the 2G Enterprises Superconducting Rock Magnetometer at MIT to identify the characteristic magnetization components. An AF demagnetization sequence with maximum field of 145 mT and demagnetization/measurement intervals of 1 mT was performed on the thin sections.

4. Results

4.1. Petrology and Geochemistry of Rock Samples

The microtextural analysis and thin section TIMA EDS mapping of the least altered samples (GM-LSH-96, -74) indicate that peridotite hydration had reached completion and the entire magmatic mineral assemblage was replaced by massive serpentine (~88 area %) (Figure 3 and Figure S2 in Supporting Information S1; Table 1). Both serpentinite samples contain additional, up to 2 mm wide, bastite intergrowths of talc (~7%) and dolomite (0.3% and 2.8%) after primary clinopyroxene (Figure 3a). The bulk serpentinite thin section contents of magnetite are 1.5% (GM-LSH-96) and 3.0% (GM-LSH-74), and GM-LSH-96 contains an additional 0.2% of pentlandite ($(Fe,Ni)_9S_8$) (Figure 3b). The magnetite grain size is highly variable. Image analysis based on 2D thin section SEM-EDS imaging indicates that 50% of the grains are smaller than 75 μm^2. The cumulative frequency of magnetite cross-sectional areas shows relatively similar distributions in the serpentinite and listvenite, while in the soapstone larger magnetite grains are relatively more abundant (Figure S2 in Supporting Information S1). Talc-rich samples (GM-LSH-69 and -48) were collected from a 1-m-wide zone between the serpentinite and listvenite. GM-LSH-69 is a soapstone that contains ~77% talc, together with 11% serpentine, and ~5% of each magnesite and dolomite (Table 1; Figure 3b). Most of the serpentine occurs in aggregates together with magnesite that are enclosed in the talc matrix, and additional minor amounts of serpentine occur as isolated grains enclosed by talc (Figure 3b). Dolomite preferentially occurs as veins crosscutting serpentine-magnesite clusters. Magnetite (~0.4%) occurs also in clusters and isolated veinlets. GM-LSH-48 is soapstone that contains ~52% talc and ~36% magnesite, together with small amounts of relict serpentine (~4%) and magnetite (~0.4%; see Figure S2 in Supporting Information S1 for the statistics of grain area distributions), while dolomite is absent. Magnesite occurs in up to 2 mm wide veins and intimately intergrown with talc in the matrix. Serpentine is present as fine-grained relicts in two regions of the thin section with high talc/magnesite. Magnetite is present as isolated subhedral grains of up to 200 μm in diameter (Figures 3b and 3c).

The listvenite sample GM-LSH-39 contains ~59% magnesite and ~38% quartz, with only minor amounts of talc (~1.1%), serpentine (~0.9%), magnetite (~0.2%), and pentlandite (~0.1%) (Table 1; Figure 3b). Quartz is concentrated in up to 4 mm thick veins and as clusters in the magnesite-dominated matrix. Subhedral magnetite is coarse-grained (<350 μm) and present as inclusions in matrix magnesite and quartz (Figure 3c). Even though we observed no fuchsite in the listvenite sample used in this study, this mineral can be relatively common in other locations in Atlin (e.g., the Pictou gold showing) (see Figure 1). In summary, the thin section analyses show that magnetite contents are highest in serpentinite, intermediate in soapstone, and lowest in listvenite.

4.2. Magnetic Field Measurements

For the field survey, total magnetic field variations along the survey line were calculated from the vector magnetic measurements. The observed total field values were corrected with the removal of Earth's main field using the International Geomagnetic Reference Field (IGRF)-13 model (Alken et al., 2021) estimated at the center of the survey line. To obtain the magnetization distribution within the surveyed rock formation, we adopted the magnetic forward modeling from analytical approach taken by Talwani and Heirtzler (1964) that enables us to assess combinations of polarity and magnetic source geometry to optimize magnetic source characters. In this model, we assigned a paleoinclination and paleodeclination of ±47.68° and 65°, respectively, based on the GPlates reconstructed paleo-location of Atlin (Müller et al., 2018). We finalized the forward model parameterization by matching the calculated and observed magnetic anomalies. Our forward modeling suggests that the

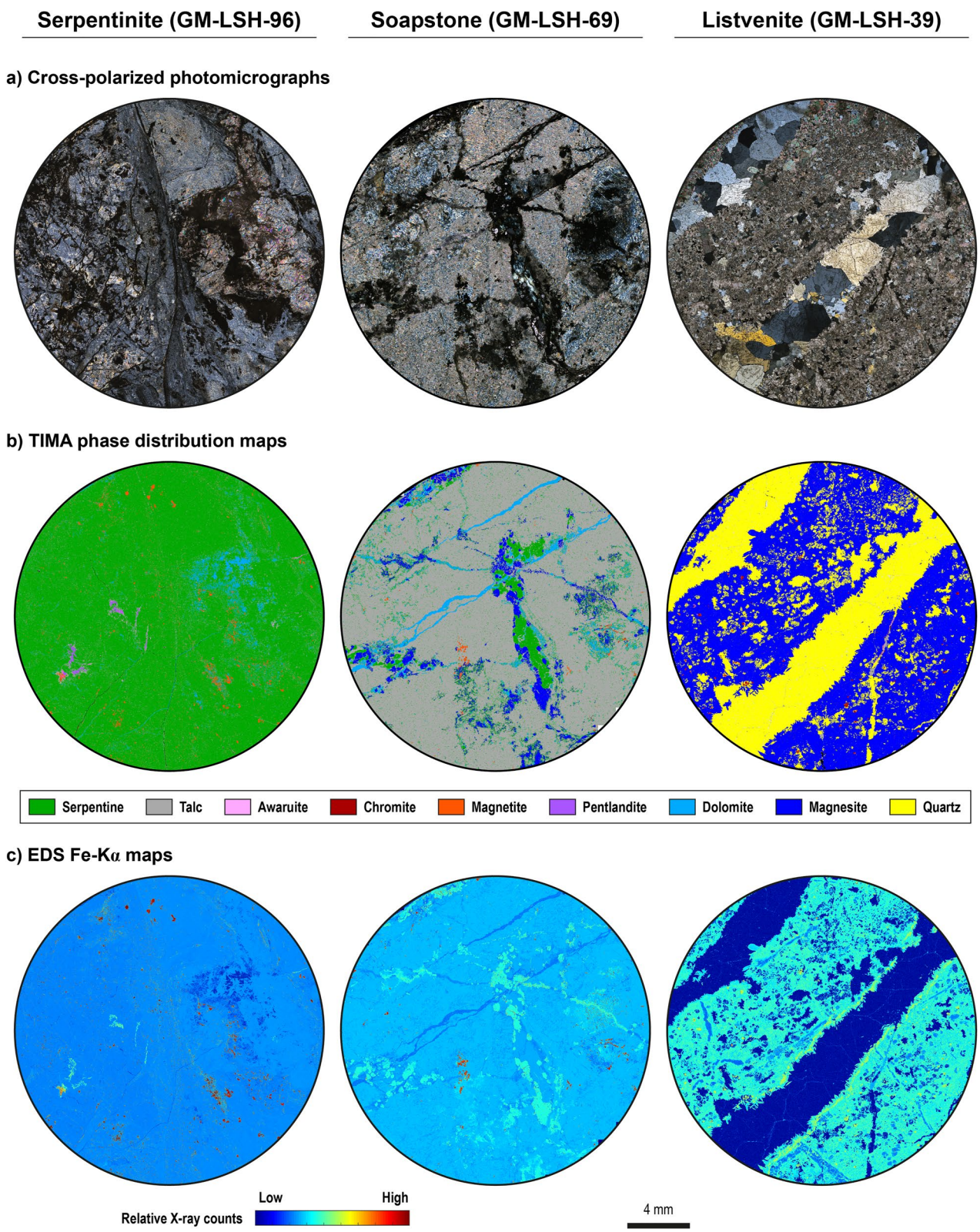

Figure 3. Microtextural observations in representative samples of the serpentinite, soapstone transition zone, and listvenite. (a) Cross-polarized full thin section photomicrographs. (b) energy dispersive spectroscopy phase maps. (c) Fe Kα element distribution maps. Note in (c) the Fe enrichment in nonoxide matrix minerals from the serpentinite to the listvenite.

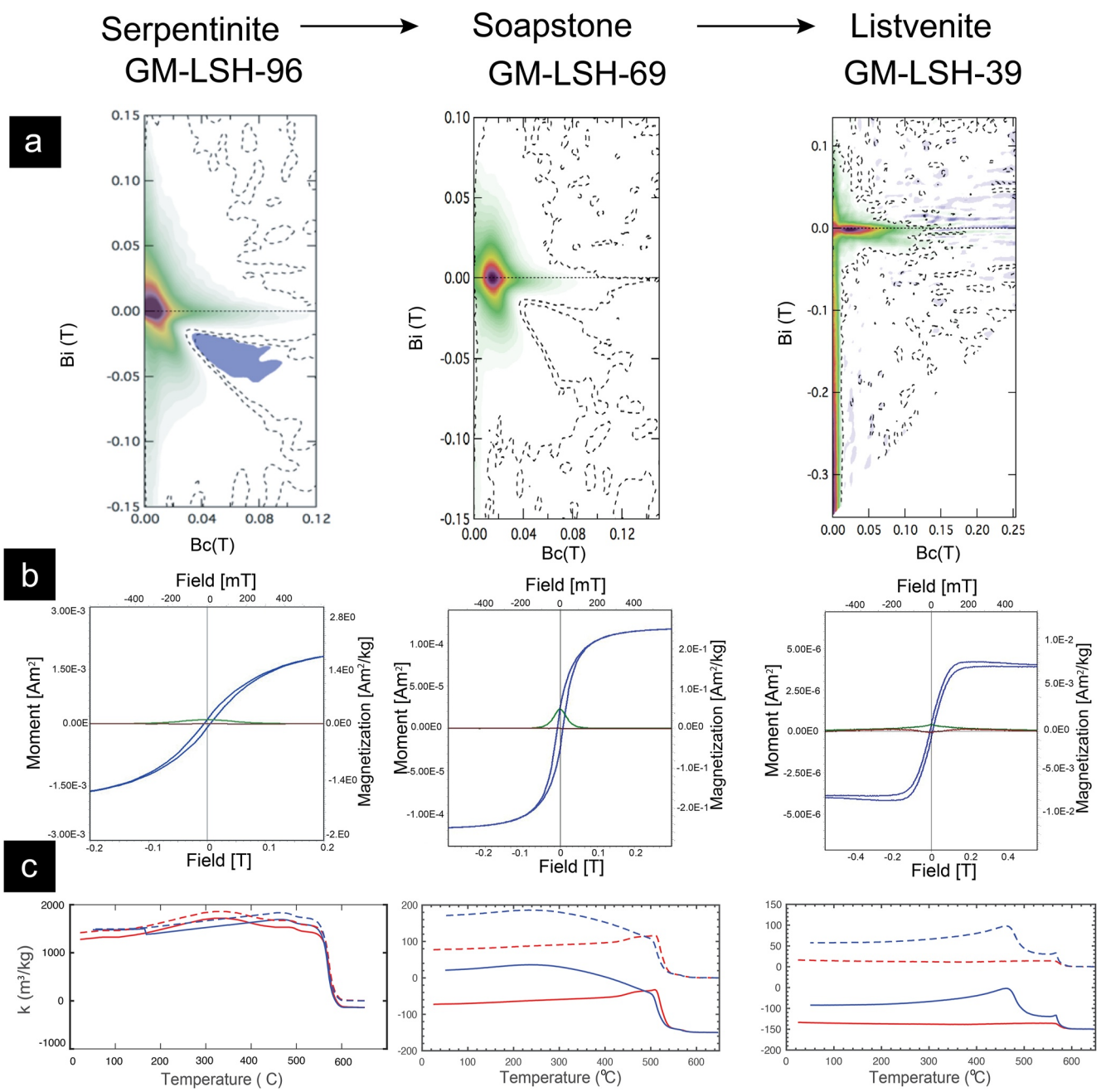

Figure 4. Rock magnetic analyses of altered peridotite samples from Atlin. (a) Processed first-order reversal curves (FORC) diagrams, (b) Hysteresis loops, and (c) Temperature-dependent susceptibility diagrams showing multiple heating (red) and cooling (blue) paths on the same sample chip. Note that to better show the FORC characteristics of each sample, we made the *x*- and *y*-axes ranges adjustable between samples. See the full suite of imagery in Figure S3 in Supporting Information S1.

ultramafic complex at Atlin mainly contains reversed polarity magnetization. The timing of such thermo-chemical remanence acquisition with a particular reversed polarity period during Early Cretaceous remains unknown (e.g., during a relatively long period of reversed polarity during the Berriasian (~M17r = 1.26 Myr)) (Gradstein & Ogg, 2020), let alone a possible thermo-chemical remanence due to syn-obduction serpentinization during mid- to late Jurassic.

Overall, the magnetization decreases approximately linearly with distance along the survey transect from a high in the serpentinite to a low in the listvenite. The trends in magnetization distribution are consistent with petrographic and geochemical mapping observations and the measured abundance of magnetite in the samples (Section 4.1).

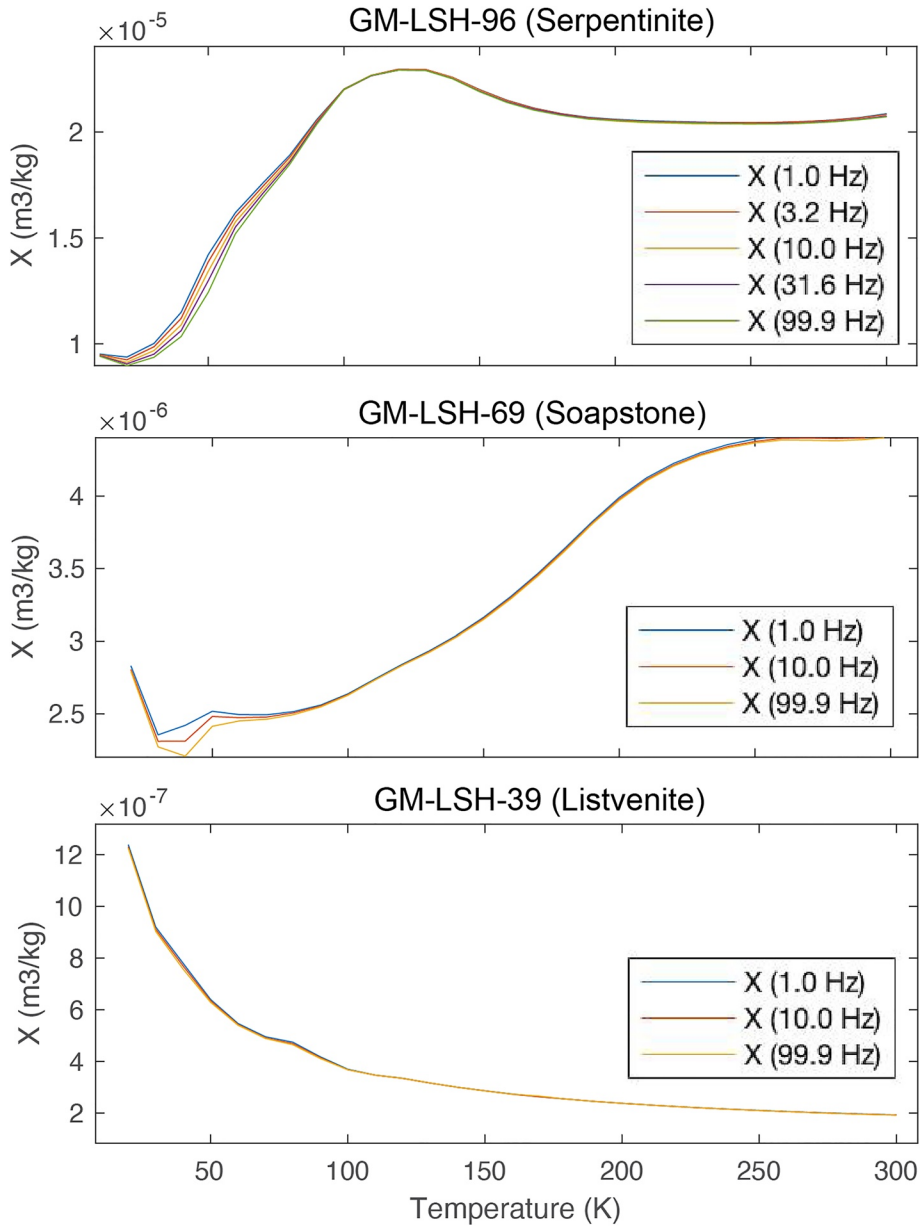

Figure 5. Frequency-dependent susceptibility measurements of three representative lithologies: serpentinite (GM-LSH-96), soapstone (GM-LSH-69), and listvenite (GM-LSH-39).

The modeled NRM magnetization is minimal for samples GM-LSH-48 and -39 (e.g., ∼0 A/m in the modeled magnetization; Figure 2b).

4.3. Rock Magnetic Analyses

Our rock magnetic analyses show a strong dichotomy within magnetic characters that correlates with the mode of alteration. For example, the serpentinite samples (GM-LSH-96 and -74) are magnetically distinct from the listvenite samples GM-LSH-48 and 39, while soapstone sample GM-LSH-69 shows a transitional character. This observation is consistent with the geochemical analyses and the EDS-based assessment of the grain size distribution (Figure S3 in Supporting Information S1).

We used FORC analysis to assess the grain size distribution of the magnetic minerals (e.g., Pike et al., 1999; Roberts et al., 2022). With their sensitivity to mineral grain size, FORC diagrams (Figure 4 and Figure S3 in

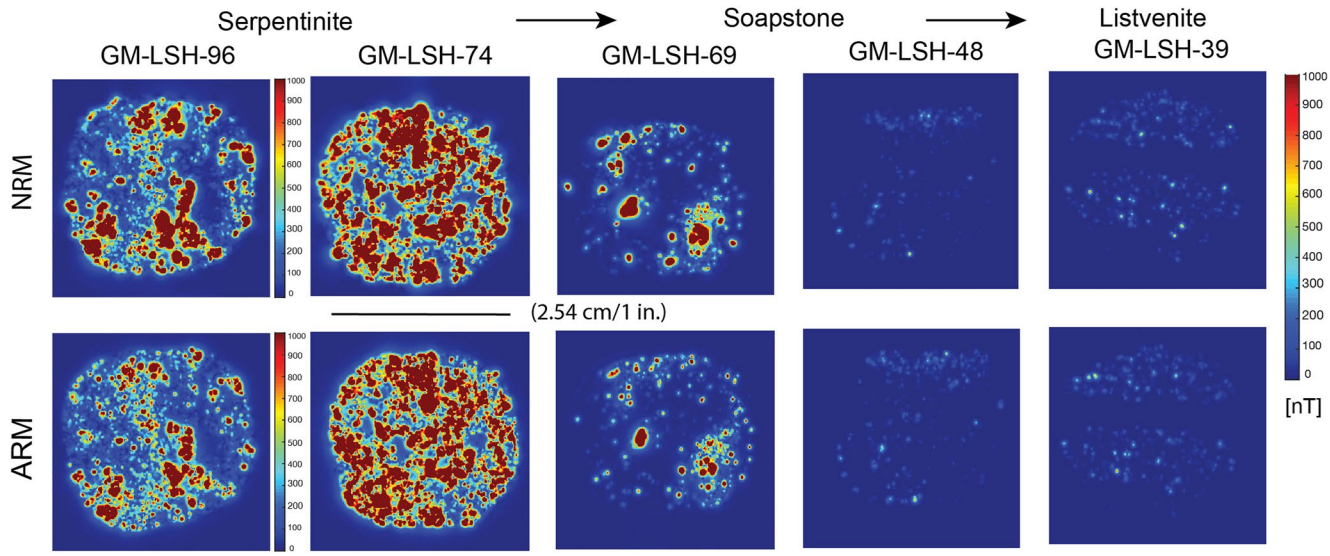

Figure 6. Scanning superconducting quantum interference device microscopy total field maps of the natural remanent magnetization and anhysteretic remanent magnetization of thin sections prepared from samples representing different stages of serpentinization and carbonation. Maps of the vertical (out of the sample plane) component of the magnetic field were measured ~200 μm above the sample and later converted to total-field estimates.

Supporting Information S1) show the coercivity characteristics of dominant mineral assemblages, exhibiting a dichotomy between the serpentinized and carbonated samples. In the FORC diagrams, the serpentinite samples display higher coercivity distributions, while the soapstone and listvenite samples display more interacting distributions, being nearly identical between GM-LSH-48 and -39. These distributions are characteristic of single domain and multidomain states of magnetic carrier minerals, respectively. Individual hysteresis loops and backfield curves further confirm a strong contrast in coercivity between serpentinite (GM-LSH-96) and listvenite (GM-LSH-39) (Figure 4b). Based on their Curie temperatures, recognized as drops in susceptibility at 580°C, magnetite is the dominant magnetic carrier mineral in samples GM-LSH-96 and -74 whereas GM-LSH-48, - 39 and −69 represent a complex mixture of magnetite and other magnetic carrier minerals, such as iron sulfide (Figure 4 and Figure S3 in Supporting Information S1, Table 1).

FDS analyses exhibit contrasts in grain domain characteristics (e.g., grain relaxation time variations at different frequencies) between serpentinite (GM-LSH-96) and listvenite (GM-LSH-39). The soapstone sample GM-LSH-69 exhibits a transitional character between serpentinite and listvenite (Figure 5). In addition, the susceptibility data of the serpentinite (GM-LSH-96) and soapstone (GMLSH-69) samples suggest the presence of superparamagnetic grains whereas no superparamagnetic grains in the listvenite (GM-LSH-39), indicating a significant change in grain size population between the alteration progress end-members (also see Figure S3 in Supporting Information S1).

4.4. Scanning SQUID Microscopy

Our SQUID microscopy results for the combined NRM and ARM measurements suggest that overall remanent magnetic field strength as determined by ARM measurements is comparable to that of NRM mapped in the field and that the total magnetic field strength its spatial association with the rock matrix depends on the lithology, consistent with the textural and chemical microanalyses. The observed NRM and ARM field strengths are highest in the serpentinite samples GM-LSH-96 and -74, weaker in the soapstone sample GM-LSH-69, and almost negligible in the soapstone sample GM-LSH-48 and the listvenite sample (GM-LSH-39). In addition, AF demagnetization of GM-LSH-96, 74, and 69 reveals the presence of NRM components, suggesting stable remanence magnetization can be held in these representative samples (Figure S4 in Supporting Information S1). In contrast, strongly carbonated samples (GM-LSH-48 and -39) exhibit incoherent, more dispersed directions throughout the demagnetization steps, highlighting the dichotomy between serpentinite and carbonate. Some of the AF demagnetization sequences on the thin sections produced results that show similarity to some multicomponent magnetizations that have been observed in oceanic serpentinized gabbro samples (e.g., Maffione et al., 2014).

The magnetometry data suggest that the changes in abundance and grain size of magnetic carrier minerals due to fluid-rock reactions impacts magnetic field strength and, possibly, also the wavelength of magnetic signals.

5. Discussion

Magnetic remote sensing with strategic mapping operations, such as a grid and/or mowing-the-lawn underway mapping with magnetic source structure models (i.e., inversion), has proven to be a powerful tool to decipher the surface and subsurface distribution and geometries of lithological and structural contrasts, including delineating alteration zones and mineral deposits in land and marine environments (Galley et al., 2020). This approach has also been emerging to provide a first-order evaluation of changes in physical properties and the extent of serpentinization and mineral carbonation processes within mantle peridotite in remote, marine environments (e.g., Cutts et al., 2021; Szitkar et al., 2014). However, while current mapping efforts capture present-day snapshots of these chemical processes in the form of rock records, we note that their interpretation often lacks the perspective of temporal evolution. As the origin and spatial extent of in situ magnetic signals are intrinsically related to the propagation of rock alteration fronts and the resulting crystallization remanence magnetization, it is imperative to correlate alteration processes and observable magnetic signals by integrating petrological and geophysical methods in suitable natural laboratories (i.e., coherent outcrops with clearly definable alteration fronts that developed due to fluid-driven alteration in a compositional homogeneous precursor rock). This allows not only to constrain the alteration extent but also to accurately monitor (i.e., forward model) *on-going* in situ mineral alteration (carbonation and serpentinization) in, for example, currently active hydrothermal systems elsewhere. Our results from the Atlin ophiolite, in comparison with our previous studies at the Linnajavri ultramafic complex (Beinlich, John, et al., 2020; Tominaga et al., 2017), contribute to developing a magnetic monitoring approach of spatially and mechanistically related serpentinization and carbonation reactions with two aspects: (a) dimensions and scales, and (b) in situ chemical processes.

5.1. Capturing Magnetic Signal Source Characters at Multiple Scales

To date, characterization of the surface and subsurface distribution of serpentinized peridotite has been conducted at various scales using a range of geophysical approaches, including airborne potential field surveys (e.g., Ash & Arksey, 1990; Roy et al., 2009; Sánchez et al., 2014). At Atlin, earlier studies by Ash and Arksey (1990) suggest a correlation between crustal scale airborne magnetic signals and geological field relationships. They used the location of mineral deposits for their interpretation of magnetic signal distribution. More recently, Hansen et al. (2005) showed that this correlation holds true also at the outcrop scale. However, the correlation of the magnetic signal with the source, the underlying chemical processes, as well as the spatial accuracy can be refined through the combined assessment of magnetic, petrological, and textural multiscale observations (Tominaga et al., 2017).

Through integrated field and laboratory analyses of outcrop-scale and micromagnetic signals, petrological and geochemical observations, Tominaga et al. (2017) showed that amplitude and wavelength variations in associated magnetic anomalies at the Linnajavri ultramafic complex change on all scales with the progression of peridotite carbonation. This correlation is caused by the systematic formation and destruction of magnetite, the main magnetic carrier, by mineral replacement reactions at distinct steps along the reaction path from incipient, via intermediate (soapstone), to complete peridotite carbonation (listvenite). To further refine and extend the model toward global applicability requires verification in geologically similar settings to capture the full range of conceivable signal variations related to natural rock heterogeneity.

The observations at Atlin are generally consistent with those made at the Linnajavri ultramafic complex (Tominaga et al., 2017), showing that intermediate and completely carbonated peridotites are characterized by distinct magnetic signals that can be captured at both the field scale and at smaller scale in the hand specimen and thin section in the laboratory. Furthermore, the Atlin field site more clearly showcases the distinct magnetic signal obtained from purely serpentinized and carbonated (soapstone and listvenite) ultramafic rock. The observations are consistent with the previous detection of large-scale aeromagnetic lows in areas of known gold and sulfide enrichment, attributed to the localized percolation of CO_2-bearing and mineralizing hydrothermal fluids (Ash, 2001; Ash & Arksey, 1990).

However, our observations at Atlin also suggest a challenge in the scalability of anomaly characters between the field and thin-section levels unlike the more straightforward stepwise change in magnetic signals observed at the Linnajavri ultramafic complex (Figures 2, 4 and 6; cf., Tominaga et al., 2017). At Atlin, both the magnetic field strength and gravity decrease almost linearly from serpentinized to carbonated peridotite. Moreover, the

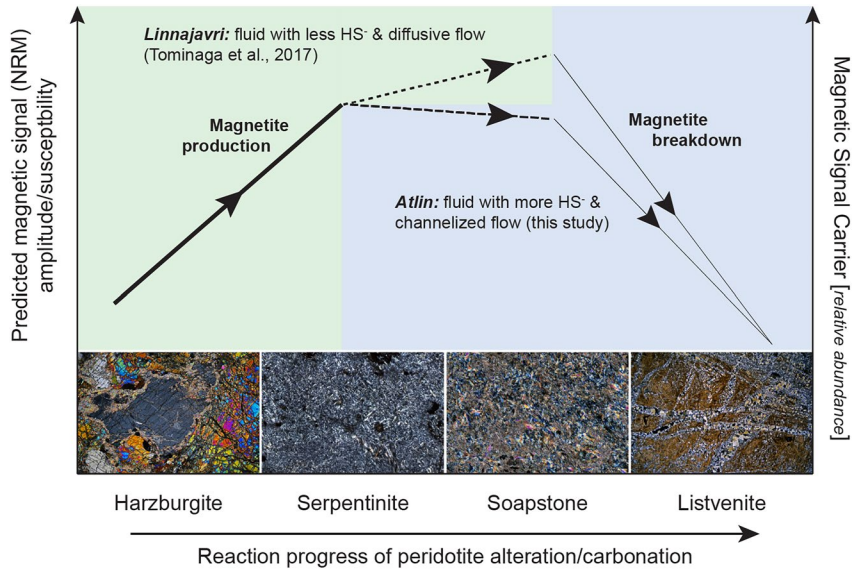

Figure 7. A schematic model depicting the relation between magnetic signal strengths and serpentinization and carbonation reaction progress. Axis scales are arbitrary. The blue zone indicates magnetite breakdown (and hence decreases in magnetic signal strength), whereas magnetite is produced in the green zone. The shown photomicrographs are representative of the different lithologies in the vicinity of the survey profile (see inset in Figure 1) and outline the evolution of olivine-bearing primary harzburgite through serpentinite, soapstone, to listvenite.

distribution of remanent magnetization calculated using induced and remanent magnetic directional components, outcrop topography, and constant layer thickness also shows such a linear trend without a distinctive contrast among lithological changes along the survey line. However, changes in these signals and magnetization distribution are seemingly overfiltered and thus challenging to directly map onto the finer observations provided by outcrop- and thin section-scale measurements. For example, with a 1 m sampling interval, the derived magnetic anomalies and magnetization distributions were unable to delineate the sharp contrast between high magnetic field strength in the serpentinite (GM LSH-96 and -74) and nearly absent total field in the carbonate-rich soapstone and listvenite (GM-LSH-48 and -39), as clearly measured by SQUID microscopy. This challenge of scalability can be attributed to the lack of a survey strategy to accommodate the three-dimensional nature and geometry of the magnetic source, which may result from anisotropic flow of the alteration fluid and hence heterogeneous 3D distribution of the alteration assemblage (cf., Galley et al., 2020). This interpretation is consistent with the highly localized nature of peridotite carbonation and mineralization at Atlin, where alteration zones are concentrated along the basal thrust (Monarch Mountain thrust) separating the ophiolite from the underlying metabasalt, and along steeply dipping ophiolite-internal faults, for example, at the Anna gold showing (Figure 1). In contrast, carbonation at Linnajavri resulted in broad, internally homogeneous alteration zones suggesting pervasive percolation of CO_2-bearing alteration fluid, likely aided by significant formation of transient, reaction-induced porosity (Beinlich, John, et al., 2020). Such broad alteration zones can be treated as quasi two-dimensional and facilitate the interpretation of magnetic mapping results assuming isotropic extension into the third dimension. Hence, to achieve effective usage of field magnetic mapping to capture structurally controlled serpentinization and carbonation in situ requires a finely sampled grid survey to recover the three-dimensionality of the magnetic source, and additional constraints on structural relationships in the investigated rock volume.

5.2. Correlating Magnetic Signal Variations With Carbonation Reactions

The correlation of magnetic with geochemical and textural observations shows that the decreasing magnetic signal strength from serpentinite to listvenite is related to the disappearance of magnetite and enrichment of talc and magnesite in Fe (Figures 3b, 3c, and 7). Along this reaction sequence, soapstone represents the transitional alteration product (see also Beinlich et al., 2012) and its magnetic signal strength is between that of serpentinite and listvenite (Figures 2 and 6). This observation contrasts with our previous observations at Linnajavri, where soapstone produces the strongest magnetic signal, resulting from the growth of additional magnetite during carbonation of the precursor serpentinite (Tominaga et al., 2017). Reaction interfaces separating the different alteration assemblages that are not accessible at

the surface represent arrested fronts that were propagating during active alteration at depths (and elevated pressure and temperature). Hence, the different assemblages can be interpreted as timeseries of in situ processes that are now observed spatially distributed, indicating that, at Atlin, soapstone formation from serpentinite destabilized magnetite. Conceptually, the soapstone forming reaction can be simplified in the $MgO\text{-}SiO_2\text{-}H_2O\text{-}CO_2$ system to:

$$\underset{\text{Serpentine}}{2\,Mg_3Si_2O_5(OH)_4} + 3\,CO_2 \rightarrow \underset{\text{Magnesite}}{3\,MgCO_3} + \underset{\text{Talc}}{Mg_3Si_4O_{10}(OH)_2} + 3\,H_2O \quad (1)$$

In principle, magnetite coexisting with serpentinite in the serpentinite could dissolve in CO_2-bearing fluid before Fe precipitates as a siderite component ($FeCO_3$) and is incorporated into magnesite. This enrichment of magnesite in Fe can be seen in, for example, zoned crystals lining the central quartz vein in Figure 3c. However, the transition of ferric to ferrous iron requires an additional oxidation reaction (of e.g., graphite), which is not observed in noncarbonated serpentinite. Thermodynamic modeling using SUPCRTBL (Zimmer et al., 2016) indicates the stability of magnetite over siderite ($FeCO_3$) (Gibbs free energy change of the reaction, $\Delta G_r >> 0$) for realistic alteration conditions (T: 200°C–400°C; P: 2–5 kbar) unless the fluid contains additional H_2S_{aq}, resulting in the concomitant formation of pyrite:

$$\underset{\text{Magnetite}}{Fe_3O_4} + 2\,H_2S_{aq} + 2\,CO_{2,aq} \rightarrow \underset{\text{Pyrite}}{FeS_2} + \underset{\text{Siderite}}{2\,FeCO_3} + 2\,H_2O \quad (2)$$

This reaction describes reductive magnetite dissolution coupled with oxidative pyrite and siderite precipitation and will spontaneously proceed at temperatures between 200°C and 400°C and 2–5 kbar pressure ($\Delta G_r < 0$) (see also Qian et al., 2010). The presence of reduced sulfur in the carbonation fluid is consistent with the occurrence of gold and sulfide mineralization in the listvenite at Atlin and in particular at the Anna gold showing near our survey transect (e.g., Ash, 2001; Ash & Arksey, 1990). Conceivably, the fluid sulfur content at Atlin was relatively higher than at Linnajavri where sulfide mineralization is absent except for minor pyrite in the listvenite, consistent with the distinct magnetic field strengths of soapstone from the two field sites.

Furthermore, Atlin and Linnajavri exhibit different alteration styles while producing similar alteration mineral assemblages. At Linnajavri, percolation of CO_2-bearing alteration fluid led to the formation of broad and internally homogeneous alteration zones that extend for hundreds of meters and are separated by sharp reaction fronts. Their distribution follows an almost ideal metasomatic zoning model, suggesting that local thermodynamic equilibrium was attained, and that pervasive fluid flow was likely aided by a transient reaction-induced permeability increase (Beinlich et al., 2012; Beinlich, John, et al., 2020). Upstream magnetite breakdown reactions (Equation 2) will effectively remove dissolved sulfur from the fluid, hence stabilizing magnetite in the downstream alteration assemblage. In contrast, the Atlin listvenite is present as spatially restricted alteration selvages around ophiolite-internal faults (e.g., at the Anna gold showing) and along the basal thrust (at e.g., the Pictou gold showing) with only thin and sporadically distributed pockets of transitional soapstone alteration (Hansen et al., 2005), similar to recently described alteration zone distributions in the Semail ophiolite, Oman (Beinlich, Plümper, et al., 2020; Kelemen et al., 2022). This indicates predominantly fracture-controlled and channelized fluid flow through otherwise impermeable harzburgite allowing for a larger flux of disequilibrium fluid (i.e., fluid with sufficiently high concentrations of dissolved sulfur to effectively remove magnetite from the reacting rock). The different flow modes of alteration fluid at Atlin compared to Linnajavri may be caused by the different precursor rock mineralogy prior to CO_2-fluid infiltration, and/or a slightly lower alteration temperature (Atlin: ~250°C, see Hansen et al., 2005; Linnajavri: ~300°C). At Atlin, textural observations indicate that the alteration fluid infiltrated only partly serpentinized rock containing abundant magmatic olivine, which is absent from the precursor serpentinite at Linnajavri. If a solid mass was preserved, the replacement of olivine by quartz + magnesite would be accompanied by an increase in solid volume by ~84%, whereas the formation of the same reaction products from serpentine (antigorite) would increase the solid volume by only 9%. Even though a perfect mass conservation is a simplified endmember scenario, the different volume changes suggest a higher volume strain during the carbonation at Atlin, and may prevent the pervasive rock alteration.

6. Conclusions

Our study of the Atlin ophiolite, particularly in comparison with the Linnajavri ultramafic complex, confirms the correlation between magnetic signals, serpentinization, and carbonation processes. We argue that magnetic mapping, particularly combining high-resolution field mapping with laboratory analyses of representative rock

samples, is a globally viable approach to track the serpentinization and carbonation processes in mantle peridotite. This includes the use of static magnetic measurements as a monitoring tool for the temporal evolution of carbonation in situ throughout CO_2 injection/geological carbon sequestration experiments. If the carbonation progresses at observable rates (e.g., up to 10 cm/year in Linnajavri; Beinlich, John, et al., 2020) throughout a sizable rock volume, stationary magnetometers can be expected to be able to monitor the reaction progress.

However, the correlation of magnetic signals with chemical reactions requires additional constraints on fluid composition, since its control on magnetite stability may produce identical magnetic signals at different steps along the rock alteration reaction path (e.g., pristine peridotite compared to completely carbonated listvenite). In this case, detailed investigation on density contrast using near-source gravity surveys with a closely knitted survey pattern. Furthermore, the interpretation of remotely acquired magnetic monitoring data of the carbonation reaction progress will also require additional constraints on the mode of fluid flow (i.e., pervasive vs. channelized). Based on a comparison of Linnajavri and Atlin, we propose a refined model to describe the correlation of magnetic signal strength during the reaction progress of serpentinization and carbonation of mantle peridotite from that of Tominaga et al. (2017) (Figure 7). The consistently low magnetic field strength of listvenite from the two study sites corroborates the global applicability of magnetometry as a monitoring tool for in situ carbonation of ultramafic rock. Moreover, the difference in magnetic signal strength of the soapstone assemblage, which represents the transitional alteration assemblage at both Atlin and Linnajavri, indicates that the change in magnetic field strength at the carbonation front relative to the precursor rock can be directly linked to the formation and breakdown of magnetic carrier minerals and hence fluid composition and flow mode.

Data Availability Statement

Data used in this study are currently publicly available at https://doi.org/10.17605/OSF.IO/2ZMUE. The data are archived at the Open Science Framework (OSF: https://osf.io/2zmue/) hosted by Center for Open Science.

Acknowledgments
MT and AB thank Ian Power for sharing his knowledge during our field work in Atlin. MT and student coauthors PD and NV thank John Greene and Patrick Fulton for mentoring them in the field and during lab work. MT especially thanks the staff at IRM who assisted NV's IRM student fellowship to conduct and analyze a series of rock magnetic measurements on Atlin samples presented in this study. EAL thanks NSF SQUID microscopy development grant. Tommaso Tacchetto is thanked for help with TIMA analyses. This study is supported by NSF EAR-Geophysics 1950674 and NASA Astrobiology Institute NNA15BB02A ("Rock Powered Life"). EAL and BPW were partly supported by NSF DMS-1521765.

References

Airo, M.-L. (2002). Aeromagnetic and aeroradiometric response to hydrothermal alteration. *Surveys in Geophysics*, *23*(4), 273–302. https://doi.org/10.1023/a:1015556614694

Alken, P., Thébault, E., Beggan, C. D., Amit, H., Aubert, J., Baerenzung, J., et al. (2021). International geomagnetic reference field: The thirteenth generation. *Earth Planets and Space*, *73*(1), 49. https://doi.org/10.1186/s40623-020-01288-x

Andrew, K. (1985). *Fluid inclusion and chemical studies of gold–quartz veins in the Atlin Camp, Northwestern British Columbia*. University of British Columbia.

Ash, C. H. (1994). *Origin and tectonic setting of ophiolitic ultramafic and related rocks in the Atlin area, British Columbia (NTS 104N)* (Vol. 94). B.C. Ministry of Energy, Mines and Petroleum Resources.

Ash, C. H. (2001). *Relationship between ophiolites and gold–quartz veins in the North American Cordillera* (Vol. 108). B.C. Department of Energy, Mines and Petroleum Resources.

Ash, C. H., & Arksey, R. L. (1990). The listwanite-lode gold association in British Columbia. In *Geological fieldwork 1989, A summary of field activities and current research, Province of British Columbia* (pp. 359–364). Mineral Resources Division Geological Survey Branch.

Bach, W., Paulick, H., Garrido, C. J., Ildefonse, B., Meurer, W. P., & Humphris, S. E. (2006). Unraveling the sequence of serpentinization reactions: Petrography, mineral chemistry, and petrophysics of serpentinites from MAR 15°N (ODP Leg 209, Site 1274). *Geophysical Research Letters*, *33*(13), L13306. https://doi.org/10.1029/2006GL025681

Beinlich, A., & Austrheim, H. (2012). In situ sequestration of atmospheric CO_2 at low temperature and surface cracking of serpentinized peridotite in mine shafts. *Chemical Geology*, *332–333*, 32–44. https://doi.org/10.1016/j.chemgeo.2012.09.015

Beinlich, A., John, T., Vrijmoed, J. C., Tominaga, M., Magna, T., & Podladchikov, Y. Y. (2020). Instantaneous rock transformations in the deep crust driven by reactive fluid flow. *Nature Geoscience*, *13*(4), 307–311. https://doi.org/10.1038/s41561-020-0554-9

Beinlich, A., Plümper, O., Boter, E., Müller, I. A., Kourim, F., Ziegler, M., et al. (2020). Ultramafic rock carbonation: Constraints from listvenite core BT1B, Oman Drilling Project. *Journal of Geophysical Research: Solid Earth*, *125*(6), e2019JB019060. https://doi.org/10.1029/2019JB019060

Beinlich, A., Plümper, O., Hövelmann, J., Austrheim, H., & Jamtveit, B. (2012). Massive serpentinite carbonation at Linnajavri, N–Norway. *Terra Nova*, *24*(6), 446–455. https://doi.org/10.1111/j.1365-3121.2012.01083.x

Cannat, M. (1996). How thick is the magmatic crust at slow spreading oceanic ridges? *Journal of Geophysical Research*, *101*(B2), 2847–2857. https://doi.org/10.1029/95JB03116

Cutts, J. A., Steinthorsdottir, K., Turvey, C., Dipple, G. M., Enkin, R. J., & Peacock, S. M. (2021). Deducing mineralogy of serpentinized and carbonated ultramafic rocks using physical properties with implications for carbon sequestration and subduction zone dynamics. *Geochemistry, Geophysics, Geosystems*, *22*(9), e2021GC009989. https://doi.org/10.1029/2021GC009989

Daae, F. L., Økland, I., Dahle, H., Jørgensen, S. L., Thorseth, I. H., & Pedersen, R. B. (2013). Microbial life associated with low-temperature alteration of ultramafic rocks in the Leka ophiolite complex. *Geobiology*, *11*(4), 318–339. https://doi.org/10.1111/gbi.12035

Dunlop, D., & Özdemir, Ö. (1997). *Rock magnetism: Fundamentals and frontiers*. Cambridge University Press. https://doi.org/10.1017/CBO9780511612794

Frost, B. R. (1985). On the stability of sulfides, oxides, and native metals in serpentinite. *Journal of Petrology*, *26*(1), 31–63. https://doi.org/10.1093/petrology/26.1.31

Frost, B. R., & Beard, J. S. (2007). On silica activity and serpentinization. *Journal of Petrology*, *48*(7), 1351–1368. https://doi.org/10.1093/petrology/egm021

Galley, C. G., Jamieson, J. W., Lelièvre, P. G., Farquharson, C. G., & Parianos, J. M. (2020). Magnetic imaging of subseafloor hydrothermal fluid circulation pathways. *Science Advances*, *6*(44), eabc6844. https://doi.org/10.1126/sciadv.abc6844

Gradstein, F. M., & Ogg, J. G. (2020). Chapter 2—The Chronostratigraphic scale. In F. M. Gradstein, J. G. Ogg, M. D. Schmitz, & G. M. Ogg (Eds.), *Geologic time scale 2020* (pp. 21–32). Elsevier. https://doi.org/10.1016/B978-0-12-824360-2.00002-4

Hansen, L. D., Dipple, G. M., Gordon, T. M., & Kellett, D. A. (2005). Carbonated serpentinite (listwanite) at Atlin, British Columbia: A geological analogue to carbon sequestration. *The Canadian Mineralogist*, *43*(1), 225–239. https://doi.org/10.2113/gscanmin.43.1.225

Harrison, R. J., & Feinberg, J. M. (2008). FORCinel: An improved algorithm for calculating first-order reversal curve distributions using locally weighted regression smoothing. *Geochemistry, Geophysics, Geosystems*, *9*(5), Q05016. https://doi.org/10.1029/2008GC001987

Johnston, S. T., & Borel, G. D. (2007). The odyssey of the Cache Creek terrane, Canadian Cordillera: Implications for accretionary orogens, tectonic setting of Panthalassa, the Pacific superwell, and break-up of Pangea. *Earth and Planetary Science Letters*, *253*(3–4), 415–428. https://doi.org/10.1016/j.epsl.2006.11.002

Jørgensen, S. L., & Zhao, R. (2016). Microbial inventory of deeply buried oceanic crust from a young ridge flank. *Frontiers in Microbiology*, *7*, 820. https://doi.org/10.3389/fmicb.2016.00820

Kelemen, P. B., Carlos de Obeso, J., Leong, J. A., Godard, M., Okazaki, K., Kotowski, A. J., et al. (2022). Listvenite formation during mass transfer into the leading edge of the mantle wedge: Initial results from Oman Drilling Project hole BT1B. *Journal of Geophysical Research: Solid Earth*, *127*(2), e2021JB022352. https://doi.org/10.1029/2021JB022352

Kelemen, P. B., & Matter, J. (2008). In situ carbonation of peridotite for CO_2 storage. *Proceedings of the National Academy of Sciences*, *105*(45), 17295–17300. https://doi.org/10.1073/pnas.0805794105

Klein, F., Bach, W., Humphris, S. E., Kahl, W.-A., Jöns, N., Moskowitz, B., & Berquó, T. S. (2014). Magnetite in seafloor serpentinite—Some like it hot. *Geology*, *42*(2), 135–138. https://doi.org/10.1130/g35068.1

Klein, F., Bach, W., Jöns, N., McCollom, T., Moskowitz, B., & Berquó, T. (2009). Iron partitioning and hydrogen generation during serpentinization of abyssal peridotites from 15°N on the Mid-Atlantic Ridge. *Geochimica et Cosmochimica Acta*, *73*(22), 6868–6893. https://doi.org/10.1016/j.gca.2009.08.021

Klein, F., & Garrido, C. J. (2011). Thermodynamic constraints on mineral carbonation of serpentinized peridotite. *Lithos*, *126*(3–4), 147–160. https://doi.org/10.1016/j.lithos.2011.07.020

Krevor, S. C. M., & Lackner, K. S. (2011). Enhancing serpentine dissolution kinetics for mineral carbon dioxide sequestration. *International Journal of Greenhouse Gas Control*, *5*(4), 1073–1080. https://doi.org/10.1016/j.ijggc.2011.01.006

Lorand, J. P. (1987). Cu-Fe-Ni-S mineral assemblages in upper-mantle peridotites from the Table Mountain and Blow-Me-Down Mountain ophiolite massifs (Bay of Islands area, Newfoundland): Their relationships with fluids and silicate melts. *Lithos*, *20*(1), 59–76. https://doi.org/10.1016/0024-4937(87)90024-7

Maffione, M., Morris, A., Plümper, O., & van Hinsbergen, D. J. J. (2014). Magnetic properties of variably serpentinized peridotites and their implication for the evolution of oceanic core complexes. *Geochemistry, Geophysics, Geosystems*, *15*(4), 923–944. https://doi.org/10.1002/2013GC004993

Malvoisin, B., Brunet, F., Carlut, J., Rouméjon, S., & Cannat, M. (2012). Serpentinization of oceanic peridotites: 2. Kinetics and processes of San Carlos olivine hydrothermal alteration. *Journal of Geophysical Research*, *117*(B4), 1–13. https://doi.org/10.1029/2011JB008842

Matthews, K. J., Maloney, K. T., Zahirovic, S., Williams, S. E., Seton, M., & Müller, R. D. (2016). Global plate boundary evolution and kinematics since the late Paleozoic. *Global and Planetary Change*, *146*, 226–250. https://doi.org/10.1016/j.gloplacha.2016.10.002

Mavromatis, V., Power, I. M., Harrison, A. L., Beinlich, A., Dipple, G. M., & Bénézeth, P. (2021). Mechanisms controlling the Mg isotope composition of hydromagnesite-magnesite playas near Atlin, British Columbia, Canada. *Chemical Geology*, *579*, 120325. https://doi.org/10.1016/j.chemgeo.2021.120325

McCollom, T. M., & Bach, W. (2009). Thermodynamic constraints on hydrogen generation during serpentinization of ultramafic rocks. *Geochimica et Cosmochimica Acta*, *73*(3), 856–875. https://doi.org/10.1016/j.gca.2008.10.032

Menzel, M. D., Urai, J. L., Carlos de Obeso, J., Kotowski, A., Manning, C. E., Kelemen, P. B., et al. (2020). Brittle deformation of carbonated peridodite—Insights from listvenites of the Samail Ophiolite (Oman Drilling Progject Hole BT1B). *Journal of Geophysical Research*, *125*(10), e2020JB020199. https://doi.org/10.1029/2020JB020199

Michels, A. C., McEnroe, S. A., & Fichler, C. (2018). Geophysical expression of the Leka Ophiolite, Norway, modeled from integrated gravity, magnetic and petrophysical data. *Norwegian Journal of Geology*, *98*(1), 103–125. https://doi.org/10.17850/njg98-1-07

Mihalynuk, M. G., Smith, M. T., Gabites, J. E., Runkle, D., & Lefebure, L. (1992). Age of emplacement and basement character of the Cache Creek terrane as constrained by new isotopic and geochemical data. *Canadian Journal of Earth Sciences*, *29*(11), 2463–2477. https://doi.org/10.1139/e92-193

Müller, R. D., Cannon, J., Qin, X., Watson, R. J., Gurnis, M., Williams, S., et al. (2018). GPlates: Building a virtual earth through deep time. *Geochemistry, Geophysics, Geosystems*, *19*(7), 2243–2261. https://doi.org/10.1029/2018GC007584

Natural Resources Canada. (2019). Edition 13. Retrieved from https://open.canada.ca/en/open-maps

Oufi, M., Cannat, M., & Horen, H. (2002). Magnetic properties of variably serpentinized abyssal peridotites. *Journal of Geophysical Research*, *107*(B5), 2095. https://doi.org/10.1029/2001JB000549

Pike, C. R., Roberts, A. R., & Verosub, K. L. (1999). Characterizing interactions in fine magnetic particle systems using first order reversal curves. *Journal of Applied Physics*, *85*(9), 6660–6667. https://doi.org/10.1063/1.370176

Plümper, O., Beinlich, A., Bach, W., Janots, E., & Austrheim, H. (2014). Garnets within geode-like serpentinite veins: Implications for element transport, hydrogen production and life-supporting environment formation. *Geochimica et Cosmochimica Acta*, *141*, 454–471. https://doi.org/10.1016/j.gca.2014.07.002

Power, I. M., Wilson, S. A., Harrison, A. L., Dipple, G. M., McCutcheon, J., Southam, G., & Kenward, P. A. (2014). A depositional model for hydromagnesite–magnesite playas near Atlin, British Columbia, Canada. *Sedimentology*, *61*(6), 1701–1733. https://doi.org/10.1111/sed.12124

Qian, G., Brugger, J., Skinner, W. M., Chen, G., & Pring, A. (2010). An experimental study of the mechanism of the replacement of magnetite by pyrite up to 300°C. *Geochimica et Cosmochimica Acta*, *74*(19), 5610–5630. https://doi.org/10.1016/j.gca.2010.06.035

Roberts, A. P., Heslop, D., Zhao, X., Oda, H., Egli, R., Harrison, R. J., et al. (2022). Unlocking information about fine magnetic particle assemblages from first-order reversal curve diagrams: Recent advances. *Earth-Science Reviews*, *227*, 103950. https://doi.org/10.1016/j.earscirev.2022.103950

Roy, R., Launeau, P., Carrère, V., Pinet, P., Ceuleneer, G., Clénet, H., et al. (2009). Geological mapping strategy using visible near-infrared–shortwave infrared hyperspectral remote sensing: Application to the Oman ophiolite (Sumail Massif). *Geochemistry, Geophysics, Geosystems*, *10*(2), 1–23. https://doi.org/10.1029/2008GC002154

Sánchez, M. G., Allan, M. M., Hart, C. J. R., & Mortensen, J. K. (2014). Extracting ore-deposit-controlling structures from aeromagnetic, gravimetric, topographic, and regional geologic data in western Yukon and eastern Alaska. *Interpretation*, *2*(4), SJ75–SJ102. https://doi.org/10.1190/int-2014-0104.1

Szitkar, F., Dyment, J., Fouquet, Y., Honsho, C., & Horen, H. (2014). The magnetic signature of ultramafic-hosted hydrothermal sites. *Geology*, *42*(8), 715–718. https://doi.org/10.1130/g35729.1

Talwani, M., & Heirtzler, J. R. (1964). Computation of magnetic anomalies caused by two-dimensional structures of arbitrary shape. In G. A. Parks (ed.) *Computers in the mineral industries*, (pp. 464–480). Stanford University Press.

Tominaga, M., Beinlich, A., Lima, E. A., Tivey, M. A., Hampton, B. A., Weiss, B., & Harigane, Y. (2017). Multi-scale magnetic mapping of serpentinite carbonation. *Nature Communications*, *8*(1), 1870. https://doi.org/10.1038/s41467-017-01610-4

Trommsdorff, V., & Evans, B. W. (1972). Progressive metamorphism of antigorite schist in the Bergell tonalite aureole (Italy). *American Journal of Science*, *272*(5), 423–437. https://doi.org/10.2475/ajs.272.5.423

Weiss, B. P., Lima, E. A., Fong, L. E., & Baudenbacher, F. J. (2007). Paleomagnetic analysis using SQUID microscopy. *Journal of Geophysical Research*, *112*(B9), B09105. https://doi.org/10.1029/2007JB004940

Zimmer, K., Zhang, Y., Lu, P., Chen, Y., Zhang, G., Dalkilic, M., & Zhu, C. (2016). SUPCRTBL: A revised and extended thermodynamic dataset and software package of SUPCRT92. *Computers & Geosciences*, *90*, 97–111. https://doi.org/10.1016/j.cageo.2016.02.013

References From the Supporting Information

Cattin, R., Mazzotti, S., & Baratin, L.-M. (2015). GravProcess: An easy-to-use MATLAB software to process campaign gravity data and evaluate the associated uncertainties. *Computers & Geosciences*, *81*, 20–27. https://doi.org/10.1016/j.cageo.2015.04.005

Schindelin, J., Arganda-Carreras, I., Frise, E., Kaynig, V., Longair, M., Pietzsch, T., et al. (2012). Fiji: An open-source platform for biological-image analysis. *Nature Methods*, *9*(7), 676–682. https://doi.org/10.1038/nmeth.2019